LETTERS
https://doi.org/10.1038/s41563-021-01187-w

nature materials

Check for updates

Hexagonal boron nitride as a low-loss dielectric for superconducting quantum circuits and qubits

Joel I-J. Wang[1,7]✉, Megan A. Yamoah[2,3,7], Qing Li[3], Amir H. Karamlou[1,3], Thao Dinh[2], Bharath Kannan[1,3], Jochen Braumüller[1], David Kim[4], Alexander J. Melville[4], Sarah E. Muschinske[3], Bethany M. Niedzielski[4], Kyle Serniak[4], Youngkyu Sung[1,3], Roni Winik[1], Jonilyn L. Yoder[4], Mollie E. Schwartz[4], Kenji Watanabe[5], Takashi Taniguchi[6], Terry P. Orlando[3], Simon Gustavsson[1], Pablo Jarillo-Herrero[2]✉ and William D. Oliver[1,2,3,4]✉

Dielectrics with low loss at microwave frequencies are imperative for high-coherence solid-state quantum computing platforms. Here we study the dielectric loss of hexagonal boron nitride (hBN) thin films in the microwave regime by measuring the quality factor of parallel-plate capacitors (PPCs) made of $NbSe_2$–hBN–$NbSe_2$ heterostructures integrated into superconducting circuits. The extracted microwave loss tangent of hBN is bounded to be at most in the mid-10^{-6} range in the low-temperature, single-photon regime. We integrate hBN PPCs with aluminium Josephson junctions to realize transmon qubits with coherence times reaching 25 µs, consistent with the hBN loss tangent inferred from resonator measurements. The hBN PPC reduces the qubit feature size by approximately two orders of magnitude compared with conventional all-aluminium coplanar transmons. Our results establish hBN as a promising dielectric for building high-coherence quantum circuits with substantially reduced footprint and with a high energy participation that helps to reduce unwanted qubit cross-talk.

A generalized superconducting qubit comprises Josephson junctions shunted by inductive and capacitive elements that together determine its energy spectrum[1]. While the materials comprising superconducting qubits would ideally be dissipationless, a dominant contributor to qubit decoherence is the interaction of the electromagnetic fields of the qubit with lossy bulk and interfacial dielectrics[2].

In a typical superconducting circuit, dielectric loss may occur in the tunnelling barrier of Josephson junctions and in the native oxide layers covering the many metallic and substrate interfaces of the device[3,4]. These dielectrics are typically amorphous oxides with structural defects that can be modelled as spurious two-level systems (TLSs). Although the microscopic nature of these TLSs remains to be fully understood, it has been established that the interaction between TLS ensembles and the electromagnetic fields in superconducting quantum circuits limits the coherence of qubits and the quality factor of superconducting resonators. It is also suspected that TLSs may be present at interfaces holding chemical residue left from the device fabrication processes[4,5].

State-of-the-art superconducting qubit technology has managed to mitigate the impact of dielectric loss to a degree through materials science, fabrication engineering and, primarily, improved microwave design[1]. In particular, current qubit designs employ large coplanar (lateral) capacitor pads, which serve to dilute the energy participation of amorphous interfacial dielectrics at the expense of a large form factor for individual qubits and complexities in microwave design. More importantly, the parasitic capacitive coupling between lateral capacitors, which gives rise to stray qubit–qubit coupling, tends to inadvertently increase coherent (spectator) errors[6,7], inhibiting high-fidelity quantum operations at scale. This design choice reflects the present lack of a suitable low-loss capacitor dielectric needed to make small form-factor, parallel-plate capacitors (PPCs).

Hexagonal boron nitride (hBN) is a layered van der Waals (vdW) insulator that is chemically inert and features an atomically flat interface, a crystalline structure and a lack of dangling bonds[8,9]. It provides a pristine environment for constructing devices for quantum transport, nanophotonics and graphene-based superconducting qubits[9–11]. hBN is also critical for stacking different vdW materials in any desired order while preserving the functional and structural integrity of each constituent vdW thin film. The resultant devices, called vdW heterostructures[9], exhibit structural likeness to epitaxially grown heterostructures and are readily compatible with circuit quantum electrodynamics architectures[11–13]. Although vdW materials and their heterostructures have long been anticipated to be ideal material platforms for building high-coherence quantum devices, there remains a critical—yet missing—piece of information needed for this application: the dielectric loss tangent of hBN in the presence of microwave electromagnetic fields, especially in the gigahertz regime where superconducting qubits operate. Here we directly measure the dielectric loss of hBN in the gigahertz regime using a superconducting resonator. We then corroborate that result by making a superconducting qubit with a PPC using hBN dielectric and demonstrate coherence times comparable with qubits fabricated using conventional lateral capacitors, despite being 250 times smaller in size.

We first study the microwave loss of hBN by incorporating hBN into microwave resonators. The intrinsic loss of a dielectric can be

[1]Research Laboratory of Electronics, Massachusetts Institute of Technology, Cambridge, MA, USA. [2]Department of Physics, Massachusetts Institute of Technology, Cambridge, MA, USA. [3]Department of Electrical Engineering and Computer Science, Massachusetts Institute of Technology, Cambridge, MA, USA. [4]MIT Lincoln Laboratory, Lexington, MA, USA. [5]Research Center for Functional Materials, National Institute for Materials Science, Tsukuba, Japan. [6]International Center for Materials Nanoarchitectonics, National Institute for Materials Science, Tsukuba, Japan. [7]These authors contributed equally: Joel I-J. Wang, Megan A. Yamoah. ✉e-mail: joelwang@mit.edu; pjarillo@mit.edu; william.oliver@mit.edu

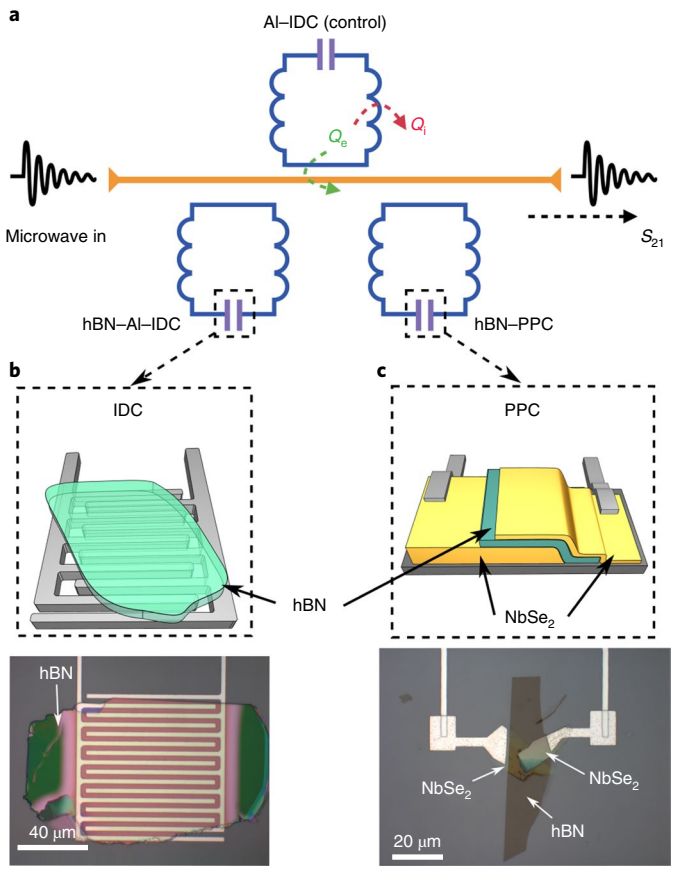

Fig. 1 | Superconducting resonators for characterizing the microwave dielectric loss of hBN. a, Schematic of the device design. A common transmission line couples inductively to three types of *LC* resonators, including a control resonator with an aluminium IDC. The external (coupling) quality factor Q_e and internal quality factor Q_i, which depend on the microwave loss properties of hBN, are extracted from the S_{21} signal measured by a vector network analyser. **b**, An hBN-coupled IDC to study the microwave loss of hBN. The hBN flake is picked up and transferred onto the IDC without any subsequent fabrication steps. **c**, An *LC* resonator consisting of a $NbSe_2$–hBN–$NbSe_2$ vdW heterostructure serving as a PPC.

characterized by its loss tangent, $\tan\delta = \mathrm{Im}[\varepsilon]/\mathrm{Re}[\varepsilon] \approx 1/Q$, where ε is the permittivity of the material and Q is the material quality factor. Figure 1a shows the schematic of our experimental design comprising lumped-element microwave resonators with a meander inductor and a capacitor that are inductively coupled to a common feedline. The quality factor of hBN can be inferred from the internal quality factor Q_i of the resonators containing hBN via the transmission coefficient S_{21} of the common feedline.

Since the electric field of the resonator driven on resonance may exist in various materials and not solely in the hBN, one must consider the 'participation' of each material and its loss. The participation ratio p_i of each material, defined as $p_i = W_{e,i}/W_{e,tot}$, where W_e is the electric field energy, is used to decompose the measured internal quality factor and its associated total loss tangent $\tan\delta_{tot}$ into a weighted sum of constituent loss tangents:

$$1/Q_i = \tan\delta_{tot} = \sum p_i \tan\delta_i, \quad (1)$$

where $\tan\delta_i$ is the loss tangent for each participating material i weighted by its participation ratio p_i.

To study the dielectric loss of hBN, we incorporate hBN crystals into two types of *LC* microwave resonators comprising of inductive (L) and capacitive (C) components: one with hBN laid on top of an interdigital capacitor (IDC) (Fig. 1b) and one with a PPC (Fig. 1c) using hBN as the capacitor dielectric. The participation ratio of hBN in each scheme is calculated using COMSOL Multiphysics (Supplementary Information section 2 and Supplementary Fig. 1), which shows that the electric fields are concentrated at the IDC and within the dielectric portion of the PPC. For the IDC resonator, an 80 μm × 80 μm capacitor and a flake thickness of roughly 500 nm yields an hBN participation ratio of around 13%. In contrast, with an hBN dielectric thickness of 10 nm and an out-of-plane dielectric constant $\varepsilon_\perp = 3.76$ (ref. [14]), the PPC for the resonator yields a capacitance of around 83 fF and an hBN participation ratio of around 66%.

Figure 1b shows a mechanically exfoliated hBN flake that is picked up and transferred onto the IDC of an aluminium microwave resonator (hBN–Al–IDC in Fig. 1a) using the standard dry-polymer technique[11,15]. The IDC design enables us to probe hBN in a relatively intrinsic or 'untouched' state because no further post-transfer fabrication is required. On the same chip, another *LC* resonator, called Al–IDC, with the same nominal resonance frequency ($f_r = 4.63$ GHz) as the unloaded (no hBN) hBN–Al–IDC resonator, is implemented as a control resonator. The device is cooled and measured in a dilution refrigerator with a base temperature of approximately 10 mK (see Supplementary Information section 3 for our measurement set-up).

We investigate the microwave loss of hBN by measuring the transmission (S_{21}, Fig. 1a) of a microwave feedline coupled to the test resonators in a hanger geometry using a vector network analyser. Figure 2a plots the internal quality factor Q_i of the hBN–Al–IDC (green data points) and Al–IDC (purple data points) resonator as a function of microwave power. The Q_i is extracted by fitting the line shape of the S_{21} signal around the resonance frequency using a numerical fit that accounts for both the internal and external Q factors (Q_i and Q_e in Fig. 1a)[16].

In the low-temperature regime ($kT \ll \hbar\omega$, where k is the Boltzmann constant, T is the temperature, $\hbar$ is reduced Planck's constant and ω is the driving-field angular frequency), the Q_i of the *LC* resonator generally increases with driving-field power, which serves to drive TLSs into saturation. Once saturated, the TLSs no longer contribute to the dielectric loss, but simply exchange energy with the resonator electromagnetic field[2,4]. In contrast, the Q_i is generally lowest at the lowest driving powers, where most TLSs are in their ground state and readily able to absorb energy from the resonator electromagnetic field. At the single-photon power level (dashed line), the hBN-coupled IDC shows a quality factor of approximately 6×10^5, whereas the Q_i of the control IDC is similar or even slightly lower (while fluctuating). Across all of the IDC devices measured, we observe that the presence of hBN does not limit the Q_i of the resonators.

To increase the participation ratio, we perform the same measurements on resonators comprising PPCs formed from hBN dielectric and $NbSe_2$, a vdW superconductor[17,18] used for the plates. The devices are fabricated as $NbSe_2$–hBN–$NbSe_2$ heterostructures (Fig. 1c). The heterostructure is assembled using dry-polymer techniques in an argon-filled glovebox to prevent oxidation at $NbSe_2$–hBN interfaces, which enables us to characterize the dielectric loss primarily given by hBN.

The quality factors Q_i versus drive power extracted from three representative PPCs are plotted in Fig. 2b,d ($f_r = 4.18$, 6.82 and 10.0 GHz, respectively). The p_{hBN} of these devices ranges from 59% to 67% and is diluted primarily by the parasitic capacitance in the meander inductor, which retains some of the electric field (Supplementary Fig. 1).

Around the single-photon power level, the Q_i of the PPC resonators (Fig. 2b–d) are approximately 2.3×10^5, 3.4×10^5 and 1.9×10^5, respectively. We average the first five data points below the single-photon limit to reduce the influence of outliers. Above

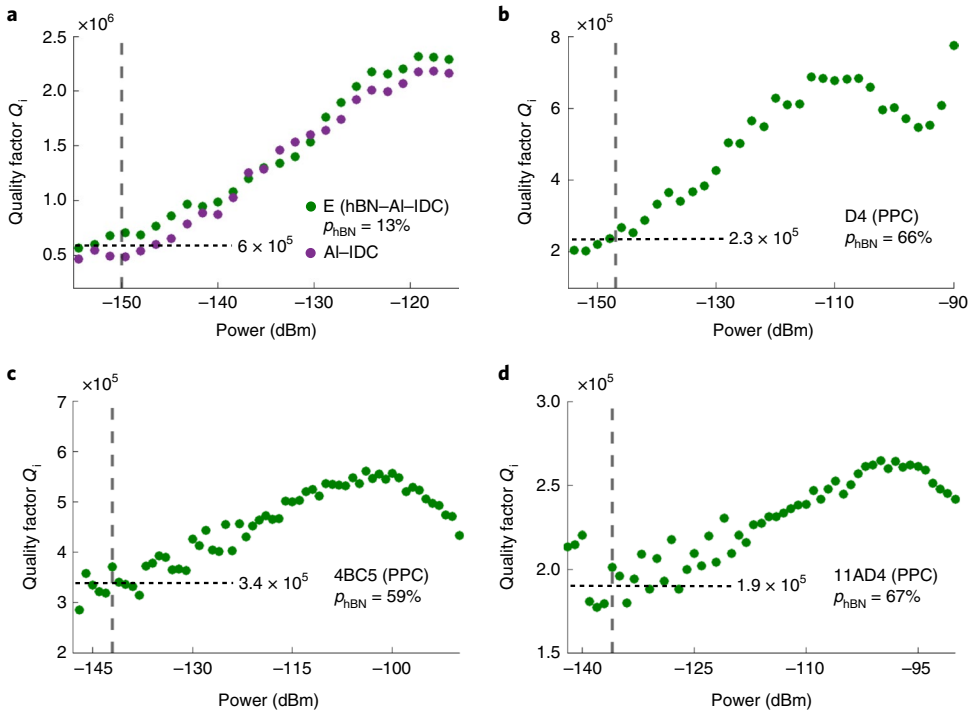

Fig. 2 | Internal quality factor Q_i of hBN-coupled *LC* resonators. a, Q_i of *LC* resonators with hBN-covered IDC (green circles) and the control Al–IDC (purple circles) plotted as a function of microwave power. The quality factors are obtained by fitting the line shape of the transmitted signal (S_{21}) around the resonance frequency[16]. At the single-photon power level (vertical dashed line), the two resonators exhibit similar Q_i. **b**–**d**, Q_i of resonators D4 (**b**), 4BC5 (**c**) and 11AD4 (**d**) with $NbSe_2$–hBN–$NbSe_2$ PPCs, all showing Q_i greater than 2×10^5 at the single-photon limit (vertical dashed lines). The decrease in Q_i at higher powers (greater than −100 dBm) may be attributed to a non-equilibrium distribution of quasiparticles induced by high microwave power and effective electron temperature[19].

the single-photon limit, Q_i generally increases with drive power until it declines at the higher power regime (at around −110 dBm). This behaviour is reminiscent of observations in aluminium resonators attributed to a non-equilibrium distribution of quasiparticles induced at high microwave drive powers that results in an additional power-dependent loss channel[19]. Given the higher participation of the hBN in the PPC configuration, a more accurate measure of the hBN material quality factor can be extracted. We estimate the hBN loss tangent $\tan\delta_{hBN}$ by decomposing the total loss as $\tan\delta_{tot} = 1/Q_i = p_{hBN}\tan\delta_{hBN} + p_r\tan\delta_r$, where p_r and $\tan\delta_r$ denote the participation ratio and loss tangent of the rest of the circuit, respectively. To calculate the worst-case upper bound of $\tan\delta_{hBN}$, we can attribute all of the loss to the hBN, that is, by assuming $\tan\delta_r = 0$. The resulting upper bound for $\tan\delta_{hBN}$ is obtained by dividing $\tan\delta_{tot}$ by p_{hBN}, which yields 6.7×10^{-6}, 5.0×10^{-6} and 7.8×10^{-6}, respectively. This directly translates to a worst-case lower bound for the hBN quality factor: $Q_{hBN} \geq 1.5\times10^5$, 2.0×10^5 and 1.3×10^5, respectively. Across all 11 measured PPC devices, eight exhibit quality factors $Q_i = 2\pi f_{01}T_1$ between 1×10^5 and 3×10^5, corresponding to an energy relaxation time T_1 between 3.9 and 12 µs, assuming a resonance frequency $f_{01} = 4$ GHz for the resonators. Measurement results from additional PPC samples can be found in Supplementary Information section 4.

hBN as a low-loss dielectric offers a promising opportunity to construct high-coherence superconducting qubits with small layout geometries. A PPC with low-loss hBN dielectric features high specific capacitance (capacitance per unit area) and maintains the capacitor electric field within a small volume consisting of high-quality hBN dielectric. Figure 3a shows such a circuit with three PPC-shunted transmons and one conventional transmon qubit with an aluminium lateral capacitor, each coupled to an individual readout resonator and sharing a common microwave feedline. The PPC-shunted transmons are constructed on a silicon chip with prefabricated aluminium circuit elements, including the transmission line, readout resonators, Josephson tunnel junctions and the aluminium transmon (Fig. 3a–c). The $NbSe_2$–hBN–$NbSe_2$ capacitors are then integrated into the circuit using the same approach as the resonator devices. The target capacitance of each PPC is 90 fF, with hBN thickness ranging from 10 to 30 nm for the corresponding plate areas spanning 27 to 80 µm^2. The hBN PPC is about 250 times smaller than the lateral capacitor of the aluminium transmon (area, $\sim2\times10^4$ µm^2 in our device) that dominates the footprint of typical Xmon-type geometry[20], while achieving energy participation ranging from 76.8% to 91.0% (Table 1).

We perform time-domain measurements of fixed-frequency and flux-tunable PPC-shunted transmons in the same measurement set-up as the resonator measurements. The fixed-frequency design allows us to probe the microwave loss of hBN-based capacitors independent of the magnetic flux-noise in the system, whereas the tunable-frequency design enables us to assess dephasing noise due to the introduced susceptibility to magnetic flux noise. Although $1/f$ magnetic flux noise is generally associated with dephasing, noise at the qubit frequency may also contribute to energy decay (loss)[21].

Figure 4a plots the excited-state probability of a fixed-frequency PPC-shunted transmon (device ID, NT-PPCQ3) initially prepared in its excited state as a function of pulse delay, from which we extract the energy relaxation time $T_1 = 24.4$ µs. In Fig. 4b, we show Ramsey interference fringes, from which we obtain the decoherence time $T_2^* = 25.1$ µs. In addition, this device has a mean T_1 of 17.9 µs and a mean T_2^* of 17.2 µs when averaged over 64 separate measurements within a 12 h window (Fig. 4a,b, inset histograms). The coherence times of this best-performing fixed-frequency PPC-shunted

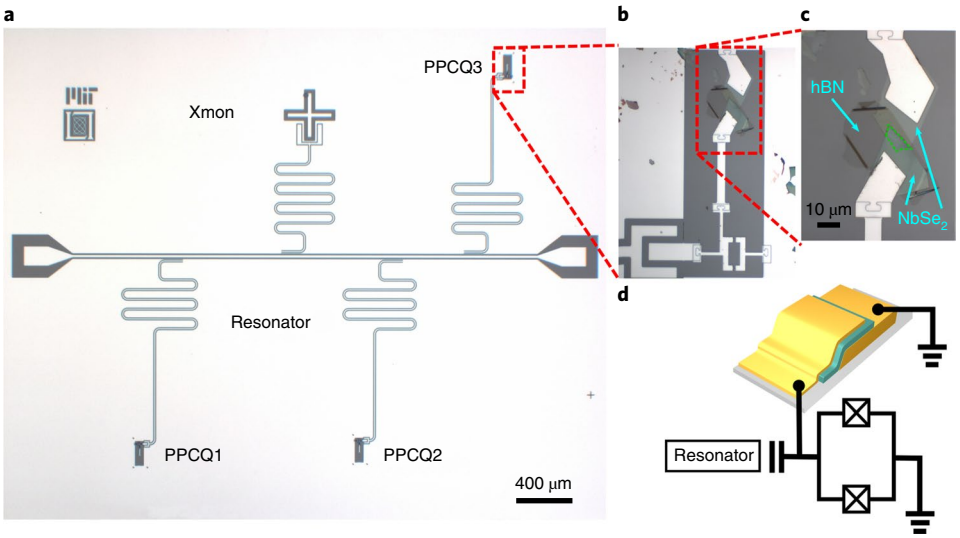

Fig. 3 | Transmon qubits shunted by PPCs. a, Optical image of a PPC-shunted transmon chip. Four qubits, including three PPC-shunted transmon qubits (PPCQ1–3) and one standard Xmon qubit, share a common line for readout and qubit control. All aluminium parts, except for the bridging electrodes connecting the PPC to the rest of circuit, are prefabricated before transferring the vdW heterostructures. **b**, Zoom-in image of the PPC-shunted transmon qubit, showing the superconducting quantum interference device made of Al–AlO_x–Al tunnel junctions. **c**, PPC used in the PPC-shunted transmon qubit. The capacitance is defined by the overlap region (~54 μm²) marked by the dashed line. **d**, Schematic of the flux-tunable PPC-shunted transmon qubit.

Table 1 | Characteristics of transmon qubits shunted by PPCs and conventional Xmon qubits

Device	f_{01} (GHz)	$\alpha/2\pi$ (MHz)	T_1 (μs)			$\bar{Q}$ (10^3)	T_2^* (μs)			p_{hBN} (%)	t_{hBN} (nm)	A_{PPC} (μm²)
			Best	Mean	s.d.		Best	Mean	s.d.			
Fixed-frequency transmons												
NT-Xmon	3.69	222.2	51.6	49.0	1.70	-	73.6	38.2	13.8	-	-	-
NT-PPCQ1	3.61	206.6	22.4	14.9	2.84	338.2	21.2	9.1	5.12	76.8	30	97.0
NT-PPCQ2	3.50	154.0	4.6	2.0	0.84	43.4	4.3	2.7	0.67	91.0	10	174.9
NT-PPCQ3[a]	3.99	191.2	24.4	17.9	3.03	448.6	25.1	17.2	3.55	82.7	21	75.3
Flux-tunable transmons												
T-Xmon	3.80	212.6	52.9	45.5	3.44	-	5.36	4.93	0.16	-	-	-
T-PPCQ1[a]	3.82	230.0	16.1	12.1	1.70	290.6	17.1	8.34	2.61	81.0	24	68.0
T-PPCQ2	3.47	174.0	3.65	1.94	0.46	42.3	5.50	2.67	0.76	82.8	21	78.5

[a]Fixed-frequency and tunable transmons discussed in the main text. The thickness of hBN (t_{hBN}) is obtained by AFM, and the PPC area (A_{PPC}) is defined by the overlapping region of each $NbSe_2$–hBN–$NbSe_2$ stack.

qubit are approximately within a factor of 2–3 of those from the fixed-frequency aluminium transmon on the same chip, with a mean (best) $T_1 = 49.0\,(51.6)\,\mu s$ and $T_2^* = 38.2\,(73.6)\,\mu s$. We also characterize T_1 as a function of qubit transition frequency f_{01} of a flux-tunable PPC-shunted transmon (Fig. 4c, device ID, T-PPCQ1). As shown in Fig. 4d, the T_1 of such flux-tunable qubits tends to grow, albeit with temporal fluctuations, as the f_{01} decreases, a trend consistent with the qubit coupling capacitively to the dielectric and with Fermi's golden rule[22].

The coherence times and relevant parameters for both fixed-frequency and flux-tunable PPC-shunted qubits are summarized on Table 1. We emphasize that the coherence times of the best-performing PPC-shunted qubits, for either fixed-frequency or flux-tunable designs, are comparable to the standard aluminium qubit on the same chip while being more than 250 times smaller in size. The mean quality factors of the PPC-shunted qubits, estimated by presuming the slightly anharmonic qubits are harmonic oscillators, range from 4.2×10^4 to 4.5×10^5 and are consistent with the PPC quality factor characterized in the *LC* resonator (Fig. 2).

The device-to-device variation in coherence times in superconducting qubit devices is typically attributed to TLSs residing in circuit elements such as Josephson junctions and shunting capacitors. For hBN PPCs, both the materials and the associated fabrication processes could introduce TLSs into the heterostructures. For example, the dry-polymer-based stacking approach may form randomly distributed pockets filled with air or hydrocarbons between different layers[23]. These trapped materials, along with deformations of the layered materials, give rise to structural inhomogeneity that would enhance the dielectric loss in regions with high energy participation. In addition, the entire fabrication process, which incorporates the vdW heterostructures into the superconducting circuit, involves a series of thermal cycling and nanofabrication steps, which may undermine the quality factor of prefabricated elements such as Josephson junctions and resonators. It is therefore conceivable that our range of extracted hBN quality factor values—already a worst-case lower bound due to the assumption that all observed loss came from the capacitor—should be furthermore treated as a lower bound for the intrinsic hBN crystals and associated vdW

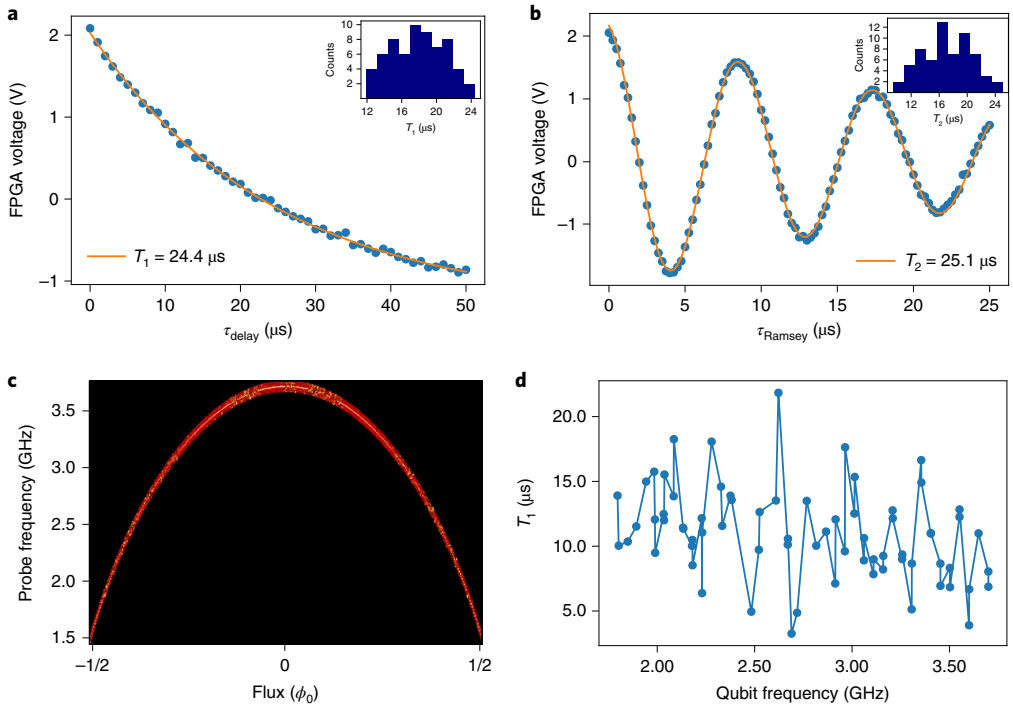

Fig. 4 | Characterization of fixed-frequency and flux-tunable transmon qubits shunted by PPCs. a, Energy relaxation time T_1 measurement of a fixed-frequency PPC-shunted transmon device (NT-PPCQ3). The fitting of the qubit population to an exponential decay function yields $T_1 = 24.4\,\mu s$. Inset: histogram from 64 averaged measurements taken over 12 h with T_1 ranging between 12 and 24 μs. **b**, Ramsey measurement of a fixed-frequency PPC-shunted transmon device (NT-PPCQ3). The dephasing time T_2^* of 25.1 μs is obtained by fitting to the function $\exp(-\tau_{Ramsey}/T_2^*) \times \cos(2\pi\Delta f \times \tau_{Ramsey})$. Inset: histogram from 64 averaged measurements taken over 12 h with T_2^* ranging between 10 and 24 μs. **c**, Energy spectrum of a flux-tunable PPC-shunted transmon device (T-PPCQ1). **d**, T_1 of a flux-tunable PPC-shunted transmon device (T-PPCQ1) measured as a function of qubit frequency. The T_1 shows an ascending trend as the qubit frequency decreases.

heterostructures. Moreover, we observe no evident correlations between Q_i values and dimensional parameters (the hBN thickness and the PPC area) from measuring 16 PPC devices (11 in *LC* resonators and five in the PPC-shunted transmon qubits) in this experiment (Table 1 and Supplementary Fig. 3). We attribute this feature and the lower loss as compared to amorphous BN (ref. [24]) to the highly crystalline bulk materials and atomically flat interfaces in the $NbSe_2$–hBN–$NbSe_2$ heterostructures. We predict that it will be possible to improve the coherence of PPC-shunted qubits or other vdW-based qubits by engineering the fabrication steps to reduce their impact on the materials.

In summary, we have characterized the microwave loss of hBN using resonators and qubits comprising hBN capacitors. The $NbSe_2$–hBN–$NbSe_2$ heterostructure, operated as a PPC in a superconducting *LC* circuit, exhibits an intrinsic quality factor up to 3.4×10^5 at the single-photon limit, indicating comparable or even better performance than that of epitaxially grown lumped-element devices previously reported[25–27]. The transmon qubits made with hBN PPCs exhibit coherence times up to 25 μs, comparable to an aluminium Xmon qubit fabricated on the same chip. Our results demonstrate that hBN is a relatively high-quality, low-loss dielectric that can be employed to build high-coherence quantum devices in the circuit quantum electrodynamics architecture. In addition, qubits shunted with hBN PPCs feature a single-qubit footprint smaller by at least two orders of magnitude than conventional lateral capacitor designs, while containing up to 91% of electric field energy between the parallel plates. We emphasize that this demonstration suggests that high-quality, lumped-element devices may be built with vdW heterostructures to mitigate unwanted qubit–qubit cross-talk, which is key to realizing high-fidelity, multi-qubit operations. Of particular interest is a vdW heterostructure comprising a Josephson tunnel junction and a shunting capacitor using hBN dielectric. Such vdW-based merged-element devices possess the potential to yield high-coherence qubits with an even further reduced form factor[28,29]. Finally, with advancements in wafer-scale growth of single-crystal hBN thin films[30,31] and vdW heterostructures, one can envision using standard wafer-scale fabrication approaches to manufacture devices incorporating hBN as a substrate, a passivation layer, lumped elements such as PPCs or Josephson junctions, and even all-vdW materials platforms for extensible superconducting quantum computing schemes.

We became aware of a complimentary work[32] during the preparation of this manuscript.

Online content

Any methods, additional references, Nature Research reporting summaries, source data, extended data, supplementary information, acknowledgements, peer review information; details of author contributions and competing interests; and statements of data and code availability are available at https://doi.org/10.1038/s41563-021-01187-w.

Received: 20 September 2021; Accepted: 8 December 2021;
Published online: 27 January 2022

References

1. Kjaergaard, M. et al. Superconducting qubits: current state of play. *Annu. Rev. Condens. Matter Phys.* **11**, 369–395 (2020).
2. Martinis, J.M. et al. Decoherence in Josephson qubits from dielectric loss. *Phys. Rev. Lett.* **95**, 210503 (2005).
3. Gambetta, J. M. et al. Investigating surface loss effects in superconducting transmon qubits. *IEEE Trans. Appl. Supercond.* **27**, 1700205 (2016).

4. Müller, C., Cole, J. H. & Lisenfeld, J. Towards understanding two-level-systems in amorphous solids: insights from quantum circuits. *Rep. Prog. Phys.* **82**, 124501 (2019).
5. Woods, W. et al. Determining interface dielectric losses in superconducting coplanar-waveguide resonators. *Phys. Rev. Appl.* **12**, 014012 (2019).
6. Arute, F. et al. Quantum supremacy using a programmable superconducting processor. *Nature* **574**, 505–510 (2019).
7. Zajac, D. et al. Spectator errors in tunable coupling architectures. Preprint at https://arxiv.org/abs/2108.11221 (2021).
8. Dean, C. R. et al. Boron nitride substrates for high-quality graphene electronics. *Nat. Nanotechnol.* **5**, 722–726 (2010).
9. Geim, A. K. & Grigorieva, I. V. Van der waals heterostructures. *Nature* **499**, 419–425 (2013).
10. Caldwell, J. D. et al. Photonics with hexagonal boron nitride. *Nat. Rev. Mater.* **4**, 552–567 (2019).
11. Wang, J. I.-J. et al. Coherent control of a hybrid superconducting circuit made with graphene-based van der Waals heterostructures. *Nat. Nanotechnol.* **14**, 120–125 (2019).
12. Schmidt, F.E., Jenkins, M.D., Watanabe, K., Taniguchi, T. & Steele, G.A. A ballistic graphene superconducting microwave circuit. *Nat. Commun.* **9**, 4069 (2018).
13. Kroll, J.G. et al. Magnetic field compatible circuit quantum electrodynamics with graphene Josephson junctions. *Nat. Commun.* **9**, 4615 (2018).
14. Laturia, A., Van de Put, M. L. & Vandenberghe, W. G. Dielectric properties of hexagonal boron nitride and transition metal dichalcogenides: from monolayer to bulk. *NPJ 2D Mater. Appl.* **2**, 6 (2018).
15. Wang, L. et al. One-dimensional electrical contact to a two-dimensional material. *Science* **342**, 614–617 (2013).
16. Probst, S., Song, F. B., Bushev, P. A., Ustinov, A. V. & Weides, M. Efficient and robust analysis of complex scattering data under noise in microwave resonators. *Rev. Sci. Instrum.* **86**, 024706 (2015).
17. Xi, X. et al. Ising pairing in superconducting $NbSe_2$ atomic layers. *Nat. Phys.* **12**, 139–143 (2016).
18. Ugeda, M. M. et al. Characterization of collective ground states in single-layer $NbSe_2$. *Nat. Phys.* **12**, 92–97 (2016).
19. De Visser, P. et al. Evidence of a nonequilibrium distribution of quasiparticles in the microwave response of a superconducting aluminum resonator. *Phys. Rev. Lett.* **112**, 047004 (2014).
20. Barends, R. et al. Coherent Josephson qubit suitable for scalable quantum integrated circuits. *Phys. Rev. Lett.* **111**, 080502 (2013).
21. Yan, F. et al. The flux qubit revisited to enhance coherence and reproducibility. *Nature Commun.* **7**, 12964 (2016).
22. Schoelkopf, R., Clerk, A., Girvin, S., Lehnert, K. & Devoret, M. in *Quantum Noise in Mesoscopic Physics* (ed. Nazarov, Y. V.) 175–203 (Springer, 2003).
23. Haigh, S. et al. Cross-sectional imaging of individual layers and buried interfaces of graphene-based heterostructures and superlattices. *Nat. Mater.* **11**, 764–767 (2012).
24. Wisbey, D. S. et al. Dielectric loss of boron-based dielectrics on niobium resonators. *J. Low Temp. Phys.* **195**, 474–486 (2019).
25. Weber, S. J., Murch, K. W., Slichter, D. H., Vijay, R. & Siddiqi, I. Single crystal silicon capacitors with low microwave loss in the single photon regime. *Appl. Phys. Lett.* **98**, 172510 (2011).
26. Cho, K.-H. et al. Epitaxial Al_2O_3 capacitors for low microwave loss superconducting quantum circuits. *APL Mater.* **1**, 042115 (2013).
27. Kim, S. et al. Enhanced coherence of all-nitride superconducting qubits epitaxially grown on silicon substrate. *Commun. Mater.* **2**, 98 (2021).
28. Zhao, R. et al. Merged-element transmon. *Phys. Rev. Appl.* **14**, 064006 (2020).
29. Mamin, H. J. et al. Merged-element transmons: design and qubit performance. *Phys. Rev. Appl.* **16**, 024023 (2021).
30. Lee, J. S. et al. Wafer-scale single-crystal hexagonal boron nitride film via self-collimated grain formation. *Science* **362**, 817–821 (2018).
31. Chen, T.-A. et al. Wafer-scale single-crystal hexagonal boron nitride monolayers on Cu(111). *Nature* **579**, 219–223 (2020).
32. Antony, A. et al. Miniaturizing transmon qubits using van der Waals materials. *Nano Lett.* **21**, 10122–10126 (2021).

Publisher's note Springer Nature remains neutral with regard to jurisdictional claims in published maps and institutional affiliations.

© The Author(s), under exclusive licence to Springer Nature Limited 2022

Methods
Details about device fabrication, measurement set-ups and simulations are available in the Supplementary Information.

Data availability
The data that supports the findings of this study are available from the corresponding author upon reasonable request and with the cognizance of our US Government sponsors who funded the work.

Acknowledgements
We acknowledge helpful discussions with G. Calusine, T. Hazard, D. Klein, D. MacNeill, K. O'Brien, A. Di Paolo and A. Vepsäläinen. We thank R. Das at MIT Lincoln Laboratory for technical assistance. This research was funded in part by the US Army Research Office grant number W911NF-18-S-0116, by the National Science Foundation QII-TAQS grant number OMA-1936263, and by the Assistant Secretary of Defense for Research & Engineering via MIT Lincoln Laboratory under Air Force contract number FA8721-05-C-0002. K.W. and T.T. acknowledge support from the Elemental Strategy Initiative conducted by the MEXT, Japan (grant number JPMXP0112101001) and JSPS KAKENHI (grant numbers 19H05790 and JP20H00354). The views and conclusions contained herein are those of the authors and should not be interpreted as necessarily representing the official policies or endorsements of the US Government.

Author contributions
J.I-J.W. and M.A.Y. conceived and designed the experiment. M.A.Y. performed the microwave simulation. J.I-J.W., M.A.Y., Q.L., T.D., D.K., A.J.M., B.M.N, K.S., J.L.Y. and M.E.S. contributed to the device fabrication. J.I-J.W., M.A.Y., A.H.K., S.E.M., B.K., Y.S., J.B., S.G. and R.W. participated in the measurements. M.A.Y., J.I-J.W. and A.H.K analysed the data. K.W. and T.T. grew the hBN crystal. J.I-J.W. and W.D.O. led the paper writing, and all other authors contributed to the text. T.P.O., S.G., P.J-H. and W.D.O supervised the project.

Competing interests
The authors declare no competing interests.

Additional information
Supplementary information The online version contains supplementary material available at https://doi.org/10.1038/s41563-021-01187-w.

Correspondence and requests for materials should be addressed to Joel I-J. Wang, Pablo Jarillo-Herrero or William D. Oliver.

Peer review information *Nature Materials* thanks Mark Hersam and the other, anonymous, reviewer(s) for their contribution to the peer review of this work.

Reprints and permissions information is available at www.nature.com/reprints.